

The direct imaging search for Earth 2.0: Quantifying biases and planetary false positives

CLAIRE MARIE GUIMOND¹ AND NICOLAS B. COWAN^{1,2}

¹*Department of Earth & Planetary Sciences, McGill University, 3450 rue University, Montréal, QC Canada, H3A 0E8*

²*Department of Physics, McGill University, 3600 rue University, Montréal, QC Canada H3A 2T8*

(Revised April 4, 2018)

Submitted to AJ

Abstract

Direct imaging is likely the best way to characterize the atmospheres of Earth-sized exoplanets in the habitable zone of Sun-like stars. Previously, Stark et al. (2014, 2015, 2016) estimated the Earth twin yield of future direct imaging missions, such as LUVOIR and HabEx. We extend this analysis to other types of planets, which will act as false positives for Earth twins. We define an Earth twin as any exoplanet within half an e -folding of 1 AU in semi-major axis and $1 R_{\oplus}$ in planetary radius, orbiting a G-dwarf. Using Monte Carlo analyses, we quantify the biases and planetary false positive rates of Earth searches. That is, given a pale dot at the correct projected separation and brightness to be a candidate Earth, what are the odds that it is, in fact, an Earth twin? Our notional telescope has a diameter of 10 m, an inner working angle of $3\lambda/D$, and an outer working angle of $10\lambda/D$ (62 mas and 206 mas at $1.0 \mu\text{m}$). With no precursor knowledge and one visit per star, 77% of detected candidate Earths are actually un-Earths; their mean radius is $2.3 R_{\oplus}$, a sub-Neptune. The odds improve if we image every planet at its optimal orbital phase, either by relying on precursor knowledge, or by performing multi-epoch direct imaging. In such a targeted search, 47% of detected Earth twin candidates are false positives, and they have a mean radius of $1.7 R_{\oplus}$. The false positive rate is insensitive to stellar spectral type and the assumption of circular orbits.

Keywords: planets and satellites: detection — planets and satellites: terrestrial planets — telescopes

1. INTRODUCTION

Planned direct imaging missions would measure the reflectance spectra (Marais et al. 2002) and photometric variability (Ford et al. 2001) of Earth-sized planets orbiting in the habitable zone of nearby Sun-like stars. Many studies have shown that direct imaging is also a viable way to discover these planets (Agol 2007; Stark et al. 2016, 2015, 2014). Given enough time, a mission could discover hundreds to thousands of planets and characterize them all. In practice, there will only be enough time to characterize some of these worlds in detail. We would therefore like to distinguish between Earths and un-Earths as efficiently as possible. For although they are expected to revolutionize many aspects of planetary science, mission concepts such as LUVOIR

and HabEx are being motivated based on their ability to characterize Earth twins.

Brown (2005) presented a “photometric and obscurational single-visit completeness” method to estimate the chance, for a particular star, that a companion exoplanet is detectable during one visit given that the planet exists. In their model, “photometric” refers to the condition that the planet/star contrast must exceed the inherent instrument floor in photon counting. “Obscurational” refers to how the planet and its star must be positioned in the sky plane, such that the planet is outside the inner obscuring disk of the coronagraph or starshade. This inner working angle (IWA) is defined technically as the angle at which transmission decreases by 50%. Coronagraphs may also have an outer working angle (OWA), beyond which starlight is no longer ade-

quately suppressed. Obscuration and low contrast are the two dominant factors that could hinder a detection.¹

If one is equally interested in all planets, then an “average” mission completeness suffices, without looking at the demographics of the mission’s yield. But what if one prefers a certain kind of planet? Then we would do best to consider how a mission may be biased towards inopportune radii and semi-major axes.

While Stark et al. (2014, 2015, 2016) cared about semi-major axes between 0.7–1.5 AU, they assigned a radius of $1 R_{\oplus}$ to all planets in their completeness calculator. In reality, most planets are not the size of Earth.

We want to not only detect as many Earth twins as possible, but also know that a detected planet is an Earth twin. Many un-Earths will show up at the correct projected separation and brightness to be Earthlike. We would confuse these planets with true Earth twins, so we call them false positives.

1.1. An observation flowchart

Suppose we image a star and see a dot that we have identified as a companion, and which may be a newly-discovered Earth twin. Our options include: (i) we get a spectrum of the dot immediately; or (ii) we return to this star at a later epoch, to better constrain the companion’s semi-major axis, hoping that the planet has not become obscured by the IWA or confused with another planet in the system. If we choose option (ii), and the next image is not dissuading, then the choices are the same, *ad infinitum* until we are ready to commit to spectroscopy.² A third option is to get another image in a different filter, if one believes that colour is a useful discriminant between different types of planets (Krissansen-Totton et al. 2016), but phase-variable colours make this strategy more challenging (Cahoy et al. 2010; Mayorga et al. 2016).

Roughly speaking, one direct imaging detection provides two data: the RA and Dec of the planet relative to its host star. There are seven orbital parameters, so $\gtrsim 4$ detections are needed to establish an orbit. However, it is beyond our current scope to determine the best number of revisits, or their cadences.

Rather, our analysis considers two endmember scenarios. In “blind” searches, we assume no prior observations of the planet; our only known parameters are the

¹ Others include exo-zodiacal dust (Roberge et al. 2012) and integration time.

² A silver lining to obtaining spectra of un-Earths is that they provide a control for biosignatures, as long as we eventually determine which planets are in fact habitable.

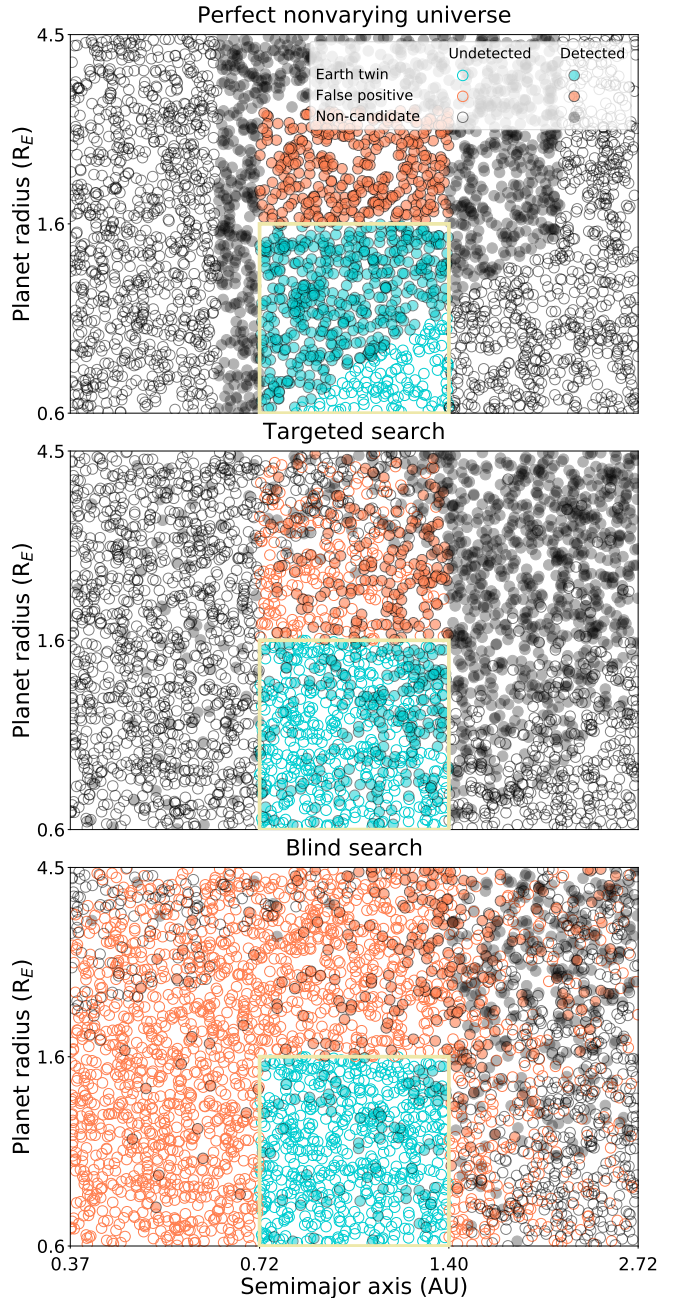


Figure 1. Demographics of detected (filled) and undetected (hollow) planets for three simulated surveys. Blue denotes an Earth twin, while orange denotes a false positive, and grey denotes a planet that would not be mistaken for an Earth twin. *Top*: a survey of an ideal universe with every star at 10 pc, and planets with face-on inclination and 30% albedo. *Middle*: a search of a universe where stellar distance and orbital inclination vary randomly; albedo can uniformly vary from 0.05 to 0.5, and the planet is imaged at gibbous phase just outside the inner working angle. *Bottom*: a search of a universe where distance, inclination, albedo, and orbital phase are random. The grid cell defining Earth twins is highlighted in yellow. Planets are distributed log-uniformly in semi-major axis and radius. Based on a simulation with stellar number density inflated by ~ 1.5 orders of magnitude to 5×10^3 stars, for visualization.

two first-order direct imaging observables of planet/star brightness contrast, ε , and projected separation, a_{proj} .

On the other hand, in “targeted” searches, we have the luxury of knowing where and when to look at each system. We assume their orbits can be predicted, based on data from either multi-epoch direct imaging, radial velocity,³ or astrometry. The Keplerian orbital fits from these observations are adequate for us to target the wanderers at gibbous phase outside the IWA (Shao et al. 2018; Butler et al. 2017; Ranalli et al. 2017).

We therefore investigate how well a direct imaging mission can distinguish between Earths and un-Earths, based solely on photometry. Particularly, we focus on the “blind” and “targeted” observation scenarios. In section 2, we describe our Monte Carlo method for simulating exoplanets and evaluating their detectabilities. Section 3 presents results, and section 4 our discussion, including a sensitivity analysis to test our assumptions.

2. MODEL DESCRIPTION

2.1. Direct imaging signal scaling

The signal from a directly imaged planet is the planet/star contrast ratio, parameterized for reflected light as

$$\varepsilon = A^* \phi_L(\alpha) \left(\frac{R}{a} \right)^2, \quad (1)$$

with planetary radius R , semi-major axis a , and apparent albedo A^* (Traub & Oppenheimer 2010). The phase function $\phi_L(\alpha)$ describes how the light scattered by a planetary atmosphere changes with the star-planet-observer angle α . For the purposes of our numerical experiment, we adopt the Lambertian phase function:

$$\phi_L(\alpha) = \frac{1}{\pi} [\sin \alpha + (\pi - \alpha) \cos \alpha]. \quad (2)$$

The phase angle is related trigonometrically to orbital phase ξ and inclination i (Traub & Oppenheimer 2010):

$$\alpha = \cos^{-1}(\cos \xi \sin i). \quad (3)$$

2.2. Conditions for detectability

Figure 1 illustrates the detection conditions for direct imaging. The top panel shows detected and undetected planets for an idealized survey in which all stars are at the same distance and all planets are in face-on orbits and have the same albedo. The only parameters allowed to vary here are planetary radius and semi-major axis. We see a distinct wedge-shaped pattern with sharp inner

and outer working angle cutoffs (left and right, respectively), and a hard-edged contrast floor (bottom right).

2.2.1. Photometric condition

For a planet to be detected, its planet/star contrast ratio must exceed the coronagraph raw contrast, $\varepsilon > \varepsilon_{\text{min}}$. We assume an optimistic LUVVOIR-esque value of $\varepsilon_{\text{min}} = 1 \times 10^{-10}$. This implicitly assumes a volume-limited survey, such that integration time per target is allotted as generously as necessary to achieve the intended signal-to-noise ratio (Stark et al. 2014).

2.2.2. Obscurational condition

Detectable planets must also have a projected separation a_{proj} falling outside the IWA of the coronagraph, and inside the OWA. That is, $a_{\text{IWA}} < a_{\text{proj}} < a_{\text{OWA}}$. Both angles are set by some multiple of λ/D , where D is telescope diameter. The IWA is often not actually a hard cutoff; it denotes the angular separation where the instrument sensitivity drops to 50% its nominal value. The approximation is nonetheless reasonable (Stark et al. 2014).⁴

Projected separation is the planet’s semi-major axis convolved with orbital elements,

$$a_{\text{proj}} = a \sqrt{\sin^2 \xi + \cos^2 \xi \cos^2 i}, \quad (4)$$

so $a_{\text{proj}} \leq a$. For now we assume circular orbits, but we test this assumption below.

The IWA limit is important for targets orbiting distant stars and/or at long wavelengths, while the OWA will pose a challenge for planets orbiting the nearest stars. The OWA is mostly of concern for blind surveys. If we already know a planet’s orbit, then we can target it at a gibbous phase with a sufficiently small projected separation (and better contrast), unless the orbital inclination is too small.

2.3. Generation of planet parameters

2.3.1. Demographics: radius and semi-major axis

Petigura et al. (2013) showed that near 1 R_{\oplus} and 365 days, the phase-space density of planets is approximately uniform in its natural logarithms (the actual variation was a factor of two). This distribution easily applies to semi-major axis due to Kepler’s Third Law.

We adopt log-uniform demographics but test the impact of this assumption below. The normalized probability densities are

$$\frac{df}{d(\ln R)} = \frac{1}{\ln(R_{\text{max}}/R_{\text{min}})} \quad (5)$$

³ Radial velocity leaves two orbital parameters unconstrained: orbital inclination and longitude of the ascending node.

⁴ The sensitivity slope has a $\Delta\lambda/D$ of ~ 1 (Guyon 2011), which is short compared to the OWA-IWA $\Delta\lambda/D$ of 7 adopted here.

and

$$\frac{df}{d(\ln a)} = \frac{1}{\ln(a_{\max}/a_{\min})}. \quad (6)$$

These describe the likelihood of a planet having radius R and semi-major axis a , given that the planet exists within that range of semi-major axes and radii. For a given star, the probability of a planet occurring in our playing field is about 7 in 10, as explained in section 2.4.3. Note that these ranges are broader than our adopted definition for Earth twins (see figure 1).

For mathematical convenience, each cell in our 3×2 a - R grid (figure 1) has a height of one e -folding in R and a width of $e^{2/3}$ in a (equal to one e -folding in period). The axis limits are chosen such that the cell defining Earth twins is centred at 1 AU and $1 R_{\oplus}$.

2.3.2. Orbital elements: phase and inclination

At a given point in time, planets can be anywhere along their orbits. We assume circular orbits, so orbital phase is uniformly distributed in $\xi \in [0, 2\pi)$, and the normalized distribution function is

$$\frac{df}{d\xi} = \frac{1}{2\pi}. \quad (7)$$

Meanwhile, inclination varies between 0 and $\pi/2$ and is uniform in $\cos i \in [0, 1]$:

$$\frac{df}{d(\cos i)} = 1. \quad (8)$$

Inclination is an unchanging property of a planet, but orbital phase, by definition, varies as the planet orbits its star. For a given inclination and semi-major axis, there exists a maximum detectable planet/star contrast, occurring each orbit, associated with a certain orbital phase. This “optimal phase” depends on our choice of phase function model. Assuming the planet is a Lambertian reflector, the optimal phase is at the gibbous phase corresponding to $a_{\text{proj}} = a_{\text{IWA}}$, or simply the fullest unobscured phase.

Analytically, the phase angle α corresponding to the optimal phase is given by substituting $a_{\text{proj}} = a_{\text{IWA}}$ into equation 4, solving for ξ , and then substituting the result into equation 3:

$$\alpha_{\text{opt}} = \sin^{-1} \left(\frac{a_{\text{IWA}}}{a} \right). \quad (9)$$

This equation has multiple roots; we are interested in the gibbous phase, so phase angle is $\alpha_{\text{opt}} \in [0, \frac{\pi}{2}]$.

2.3.3. Planetary albedo

The distribution of planetary albedos is completely unconstrained for exoplanets at large separations. We

parameterize this uncertainty by allowing A^* to vary over an order of magnitude, with uniform probability:

$$\frac{df}{dA^*} = \frac{1}{A_{\max}^* - A_{\min}^*}. \quad (10)$$

We have adopted conservative values of $A_{\max}^* = 0.5$ and $A_{\min}^* = 0.05$. As we will show in section 4.1.6, the false positive rate in a blind search is insensitive to the underlying albedo distribution, or our knowledge thereof. Shrinking the albedo range decreases the false positive rate in targeted searches, but only under certain assumptions.

2.3.4. Distance to system

We assume a constant density of stars out to the farthest distance probed r_{\max} , so the likelihood of a planetary system falling within a sphere of radius r is proportional to r^2 . The normalized probability density is therefore

$$\frac{df}{dr} = \frac{3}{r_{\max}^3} r^2. \quad (11)$$

Unfavourable orbits and/or greater distances shorten the time a planet spends between the inner and outer working angles. This decreases the number of detections, compared to a nonvarying universe (cf. top and bottom panels of figure 1). The difference between figure 1’s middle and bottom panels is due to the planet’s location in its orbit, ξ , at the time of the image. In the middle panel, we assume that the orbit of each planet is known, so we know to target stars when the planet is brightest and unobscured. On the other hand, blindly searching stars for planets is equivalent to drawing ξ from its density function (eq. 7), as in the bottom panel.

2.4. Mission parameter assumptions

2.4.1. Telescope

Diameter—Our notional telescope has a 10-m primary mirror, comparable to the proposed architecture B of LUVOIR and slightly greater than architecture A of HabEx.

Wavelength—We use a wavelength of $1.0 \mu\text{m}$ to image planets in reflected starlight. This is consistent with Stark et al. (2015); they choose $1 \mu\text{m}$ as their baseline characterization wavelength due to the water vapour feature at $0.95 \mu\text{m}$. Although searching at $0.4 \mu\text{m}$ would yield more Earth twins because the IWA would be smaller, merely finding planets at this shorter wavelength is fruitless if we cannot also characterize them.

Working angles—We adopt an IWA of $3\lambda/D$ and an OWA of $10\lambda/D$, similar to the “pessimistic” case of Stark et al. (2015).

Contrast—We assume the coronagraph has a raw contrast of $\varepsilon_{\min} = 1 \times 10^{-10}$. This threshold is often quoted as the technological goal for detection of Earth-sized planets (Dooley & Lawson 2005; Rauscher et al. 2015; Dalcanton et al. 2015). We further assume that post-processing would provide an extra order of magnitude in contrast, enabling robust detection of planets at ε_{\min} .

2.4.2. Maximum survey distance

Since we have adopted a fairly long wavelength with an accordingly large IWA, the distances at which we can probe Earth twins are limited. An Earth twin r_{\max} parsecs away, orbiting at $a_{\oplus, \max}$, would just reach the IWA at maximum elongation; any stars beyond this point could not host *detectable* Earth twins. This sets our maximum survey distance:

$$r_{\max} = \frac{a_{\oplus, \max}}{\text{IWA}} = 22.6 \text{ pc}. \quad (12)$$

This is a smaller search volume than Stark et al. (2014, 2015), who choose 50 pc as their maximum distance using telescope diameters of 4–20 m.

2.4.3. Number of targets

We assume that our survey is volume-limited, and that stars are evenly distributed across the search volume. This lets us quickly calculate the number of target stars within a sphere defined by our maximum survey distance. We use the stellar density model from Bovy (2017):

$$\frac{dN_*}{dV dM_*} = (0.016 \text{ pc}^{-3} M_{\odot}^{-1}) \left(\frac{M_*}{M_{\odot}} \right)^{-4.7}, \quad (13)$$

which we integrate over $[0.84, 1.15] M_{\odot}$.

In reality, not only are $\sim 50\%$ of Sun-like stars in binary pairs (Bate 2009), but the period distribution of binaries peaks at 10,000 days (Kroupa & Burkert 2001), about the semi-major axis of Saturn. These companion stars may pose a problem for starlight suppression. Although one could improve detection yields by a factor of ~ 2 with careful attention to coronagraph design, this is outside the scope of our current paper. We therefore eliminate half the target stars; so the number of target stars in a given simulated survey is:

$$N_* = \text{floor} \left(\frac{1.793 \times 10^{-2} r_{\max}^3}{2} \right). \quad (14)$$

This evaluates to 136 G-type stars for $r_{\max} = 22.6 \text{ pc}$. For comparison, Stark et al. (2014) report a target list of 5449 stars within 50 pc and with spectral type A

to M. Substituting these limits—excepting M-dwarfs⁵—into equation 13, we get 4937 stars.

Simulating a realistic target list, however, is not the focus of this work. We report absolute numbers primarily as a sanity check. Indeed, most of our figures and statistics come from running 100 simulated surveys to minimize Poisson noise. Results are otherwise unaffected by our chosen N_* .

2.4.4. Planet occurrence rates

To populate each star with 0 or more planets with radius $R \in [R_{\min}, R_{\max}]$ and semi-major axis $a \in [a_{\min}, a_{\max}]$, we assume an across-the-board occurrence rate density of $\Gamma = dN_p / (d \ln R d \ln P) = 0.12$ planets per star per per natural logarithmic bin in period and radius (Petigura et al. 2013; Kopparapu et al. 2018). This corresponds to an occurrence rate, η , of about 0.7 planets per star. In accordance with Poisson statistics, most stars have 0, 1, or 2 planets.

3. RESULTS

We define Earth twins in terms of planetary radius and semi-major axis. A planet orbiting a G-dwarf with $R \in [e^{-1/2}, e^{1/2}] R_{\oplus}$ and $a \in [e^{-1/2}, e^{1/2}] \text{ AU}$ is an Earth twin. Note that both ranges correspond to one e -folding; e.g., $R_{\oplus, \max} = e R_{\oplus, \min}$. This is convenient because planetary demographics are often reported as $dN / (d \ln R d \ln P)$, so the Earth twin rate is simply equal to the rate density at Earth. Our Earth twins roughly encompass the “rocky” and “super-Earth” classes of Kopparapu et al. (2018), who classify planets based on expected atmospheric chemistry. Of course, there is no evidence that all planets with the same size and orbit as Earth are anything like Earth.

3.1. Planetary false positive rates

Locating Earth twins in figure 1 is easy—they all live in the highlighted centre grid cell on the bottom row. The problem is that a single epoch of direct imaging does not yield semi-major axis and radius, but rather, projected separation and contrast ratio. Locating Earth twins on *those* axes is much trickier. We must sift through some number of un-Earthlike planets, indistinguishable from our real quarry.

We now calculate the likelihood that a planet actually is an Earth twin, given that it is detected in the contrast-separation region where an Earth twin could appear. We label this region the Earth twin candidate zone; it denotes where an Earth twin might conceivably

⁵ Only one M-dwarf, Proxima Centauri, is near enough to host Earth twins outside our adopted IWA.

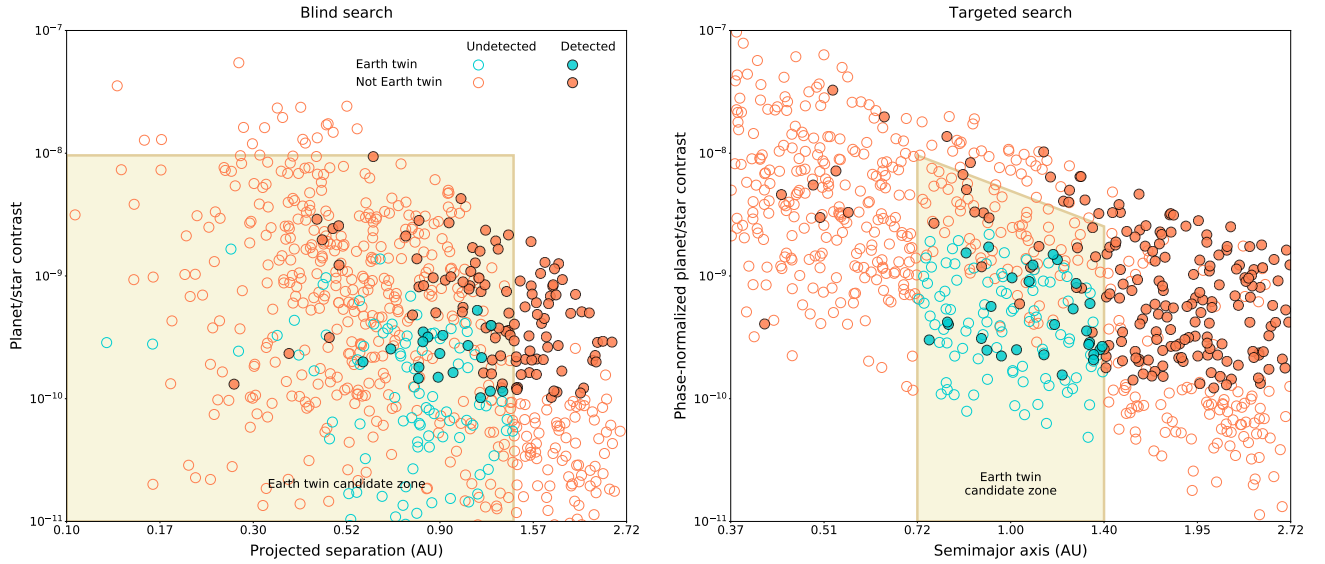


Figure 2. A comparison of survey returns in terms of the direct imaging observables, for a blind survey where planets are at random orbital phase (left), versus a survey revisiting known planets at their brightest observable phase (right). Based on a simulated survey with 10^3 stars; i.e., inflated by an order of magnitude, for visualization. Yellow regions show the “candidate zone” where a true Earth twin could possibly fall. Solid circles are detected planets, while empty circles are undetected planets. Blue circles represent Earth twins, and orange circles are un-Earths. Orange filled circles within the shaded region constitute planetary false positives: un-Earths masquerading as Earth twins.

show up in a direct imaging snapshot. The extent of the candidate zone depends on whether or not we know the planets’ orbits.

Candidates in blind searches—If we know nothing about orbital phase or inclination, then the projected separation of an Earth twin on a circular orbit is at most $a_{\oplus,\max}$, and can be as small as 0: $0 \leq a_{\text{proj}} \leq a_{\oplus,\max}$. The maximum planet/star contrast for an Earth twin is $\varepsilon_{\max} = (R_{\oplus,\max}/a_{\oplus,\min})^2$; this comes from setting the apparent albedo to unity, adopting the largest Earth-like radius, and adopting the largest possible value of $\phi_L/a^2 \approx 1.44/(\pi a_{\text{proj}}^2)$.⁶

Candidates in targeted searches—If we know the planet’s orbit, then the semi-major axis criterion for Earth twin candidacy is $a_{\oplus,\min} \leq a \leq a_{\oplus,\max}$.

To get the maximum contrast ratio, we divide ε by its Lambertian phase function, again setting A^* to unity, to compare against the stricter limit

$$\varepsilon' \leq \left(\frac{R_{\oplus,\max}}{a} \right)^2 \quad (15)$$

where ε' is the phase-standardized contrast.

⁶ Given an observed projected separation, there is a trade-off between the semi-major axis (smaller a are brighter) and orbital phase (smaller α are brighter). One can numerically solve for the maximum contrast ratio, which occurs at an orbital phase of about 63 degrees.

Un-Earthlike planets falling within the Earth twin candidate zone are false positives. They appear there for one or more of the following reasons:

1. $a < a_{\oplus,\min}$, but due to the planet’s unknown phase and inclination, we cannot rule it out as an Earth twin in gibbous or crescent phase.
2. $a > a_{\oplus,\max}$, but the planet is in gibbous or crescent phase, so its projected separation appears smaller.
3. $R > R_{\oplus,\max}$, but the planet has low albedo, decreasing its planet/star contrast to something reasonable for an Earth twin.

The degeneracy between projected separation and semi-major axis can be broken if a planet is imaged at a known orbital phase, hence ruling out the first two scenarios and ameliorating the third.

3.1.1. Quantifying the false positive rate

We essentially count the filled dots (the detected planets) in figure 2 to find the false positive rate of a survey:

$$\text{FPR} = \frac{[\# \text{ un-Earths}]_{\text{det,ETCZ}}}{[\# \text{ un-Earths}]_{\text{det,ETCZ}} + [\# \text{ Earths}]_{\text{det}}}, \quad (16)$$

where the subscript ETCZ refers to a planet falling in the Earth twin candidate zone.

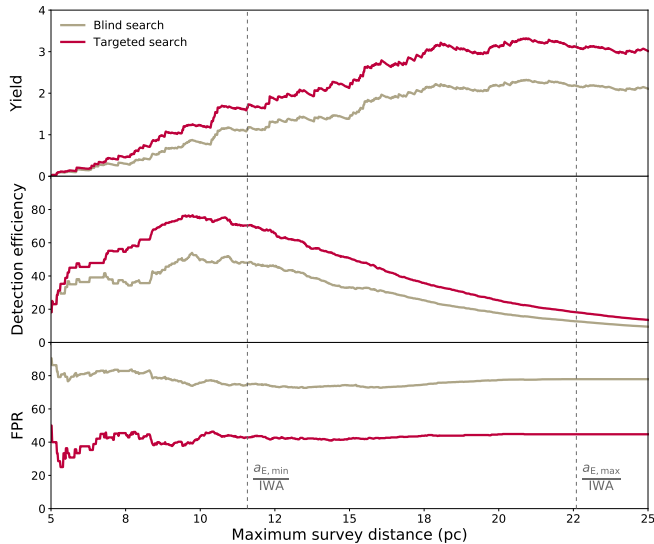


Figure 3. Search volume dependence of cumulative Earth twin yield (top), cumulative Earth twin detection efficiency (middle), and cumulative false positive rate (bottom), for blind searches (grey lines) and targeted searches (red lines). Dashed vertical lines represent the distances at which a planet’s projected angular separation would be just inside the IWA, if it orbited at $a_{\oplus,\min}$ ($r_{\max} = 11.6$ pc), and if it orbited at $a_{\oplus,\max}$ ($r_{\max} = 22.6$ pc). A targeted survey out to the leftmost dashed line would therefore detect every Earth twin bright enough to surpass the contrast floor, while no additional Earth twins could be detected beyond the rightmost dashed line. Calculated from 10^5 simulated stars, where yields are scaled to the realistic number of stars at the given r_{\max} (equation 14).

Similarly, the fraction of Earth twins detected is the number of filled teal dots to the number of teal dots:

$$f_{\text{det},\oplus} = \frac{[\# \text{ Earths}]_{\text{det}}}{[\# \text{ Earths}]_{\text{total}}}, \quad (17)$$

which we call the detection efficiency of the survey. This metric, like the false positive rate, describes the survey as a whole (cf. completeness from Brown 2005 being a function of a star). It is strongly dependent on the size of the search volume: visiting more distant stars becomes less efficient, despite the higher cumulative yield of planets (figure 3).

Table 1 presents the false positive rate for blind and targeted searches. Imaging planets at their optimal orbital phases produces a lower false positive rate because the Earth twin candidate zone is smaller. Targeting planets at their optimal phases slightly improves their planet/star contrasts and minimizes the odds of missing a planet inside the IWA.

However, knowing orbits to break degeneracy is the key here, as opposed to a better-timed observation. Merely increasing the Earth twin yield via waiting for

brighter and unobscured phases—without changing the candidate zone area accordingly—actually increases the false positive rate by a few percentage points to 81%. This is because more un-Earths are also detected alongside the Earth twins.

Table 1 also reports the biases in these searches. Most detected Earth twin candidates will have radii large enough such that they must have massive gaseous envelopes, making them sub-Neptunes (Lopez & Rice 2016; Fulton et al. 2017; Rogers 2015). Phase knowledge reduces the mean radius of detected candidates from $2.3 R_{\oplus}$ to $1.7 R_{\oplus}$ —just outside our Earth twin box.

The worst culprits are planets with radii too large to be Earthlike, but whose low albedos reduce their planet/star contrasts. For a blind search, we find that 67% of Earth twin candidates will fall in this category. This statistic drops to 47% for targets at known phase.

Semi-major axis degeneracy only creates false positives for a blind search. In this scenario, planets orbiting exterior to $a_{\oplus,\max}$ make up 27% of Earth twin candidates. Finally, planets interior to $a_{\oplus,\min}$ make up 9% of candidates. Note that these categories do not add to 100% because they are not all mutually exclusive.

Table 1. False positive rates, Earth twin detection efficiency, and biases in planetary radius R and semi-major axis a for a blind survey, versus a survey targeting planets with known orbits. False positive rate calculated via equation 16, and detection efficiency via equation 17. Based on 10^5 simulated stars.

	Blind	Targeted
False positive rate (%)	77	47
Mean Earth twin candidate R (R_{\oplus})	2.3	1.7
Mean Earth twin candidate a (AU)	1.2	1.1

As a sanity check, we can estimate Earth twin yields based on a realization scaled to a realistic number of targets, $N_* = 136$ G stars. Our simulation finds ~ 2 Earth twins in a blind search, and ~ 5 in a targeted search. Of course, our yields vary under different model assumptions, as we discuss throughout the rest of this paper.

To compare our yield results with Stark et al. (2014), we adopt their baseline mission parameters: a less forgiving telescope diameter of 8 m and IWA of $4\lambda/D$, but a more optimistic $\lambda = 550$ nm, and a larger target list of 5449 FGK stars within 50 pc. We also follow suit by fixing the occurrence rate, η_{\oplus} , at 0.1 planets per star across

Table 2. Target list sizes, number of underlying Earth twins, yields of Earth twins and un-Earths in the Earth twin candidate zone, and false positive rates under model assumptions which are relaxed one at a time. The false positive rate is quite consistent across different assumptions, despite changes in yields and target list sizes. Note that for the bottom five rows, the survey visits a dramatically different number of stars. This is due to equation 12, where any stars with maximum Earth twin semi-major axis inside the IWA are discounted from the target list. Based on 10^5 simulated stars, where yields are scaled to a realistic number of targets (as listed in columns 2 and 7). At this level of Poisson noise, the reported yields and false positive rates are precise to about ± 0.2 and $\pm 2\%$, respectively.

	Blind					Targeted				
	Stars visited	N_{\oplus} total	N_{\oplus} detected	$N_{\text{un}\oplus,\text{ETCZ}}$ detected	FPR (%)	Stars visited	N_{\oplus} total	N_{\oplus} detected	$N_{\text{un}\oplus,\text{ETCZ}}$ detected	FPR (%)
Baseline	136	16.1	2.0	7.0	77	136	16.2	5.3	4.7	47
FGK stars	420	49.2	3.9	16.2	81	434	49.5	10.9	13.9	56
Log-normal R	136	12.2	1.5	4.5	75	136	12.5	4.2	2.9	41
Log-normal P	136	33.0	4.2	10.0	70	136	32.9	11.0	9.4	46
Nonzero e	136	16.2	2.1	7.1	77	136	16.3	6.4	5.6	47
Log-normal A^*	136	16.3	2.3	7.4	76	136	16.3	6.1	4.3	41
$\lambda = 400$ nm	2126	246.1	30.4	108.2	78	2126	251.3	84.4	72.9	46
$D = 4$ m	8	1.0	0.1	0.4	77	8	1.0	0.3	0.3	46
IWA = $2\lambda/D$	235	28.1	3.6	12.1	77	235	28.3	9.5	8.2	47
OWA = $2'$	136	16.2	2.1	7.4	78	136	16.1	5.4	4.8	47
$r_{\text{max}} = a_{\oplus,\text{min}}/IWA$	18	2.1	0.9	2.9	76	18	2.1	1.9	1.4	43

our original a - R area. A targeted search under these assumptions finds ~ 5 Earth twins (plus an additional ~ 9 candidates)—consistent with the Stark et al. baseline yields of 4–16 Earth twins for a multi-visit search (roughly equivalent to our targeted scenario), depending on astrophysical and systematic noise levels. Our Earth twin definition matters here to the extent that whereas Stark et al. fixed $R = 1 R_{\oplus}$, about half of our underlying Earth twins are smaller than this. Contrast ratio goes as R^2 , so more of our simulated planets may be too faint to detect, compared to the earlier work.

4. DISCUSSION

4.1. Model assumptions

We have made several simplifying assumptions throughout this numerical study. We now evaluate how damning these assumptions may be, and how they affect our results. Table 2 summarizes our sensitivity analysis.

4.1.1. Search volume

In a volume-limited survey, one must decide on a maximum survey distance, r_{max} . There is a trade-off between detection efficiency and Earth twin yield for a given value of r_{max} (figure 3). Whereas our baseline survey sets the search volume such that a star at $r = r_{\text{max}}$ would have all of its Earth twins obscured by the IWA, we tested a simulation where the furthest star would be complete for Earth twins. We find that this assumption reduces the targeted false positive rate from 47% to

43%—not a very significant decrease—and this smaller volume may yield little-to-no Earth twins.

4.1.2. Stellar number density

We eschew rigour for analytical convenience in estimating the number of target stars in our search volume. The stellar number density parameterization from Bovy (2017) is not designed for lower-mass stars ($< 1 M_{\odot}$), and will overestimate number densities in that mass region.⁷ Other sources of error would nevertheless dominate results.

4.1.3. Stellar spectral type

Our initial assumption was that all Earth twin host stars have mass $M_* = M_{\odot}$. However, F, G, and K stars may be optimistically classified as “Sun-like”. The semi-major axis range within which a planet would receive Earth-like insolation is farther out for F stars and closer in for K stars; we therefore expect different Earth twin detectabilities, via changes in both planet/star contrast and obscuration. Here we evaluate how a realistic distribution of stellar masses would affect our results.

Our re-analysis is limited to stars at least as massive as the K5 spectral type. Habitable zone planets orbiting stars less massive than this—e.g., M-dwarfs—will not only have zero obliquity (Heller et al. 2011), but they

⁷ To get a more accurate number of G dwarfs, one should use an initial mass function below $1 M_{\odot}$ and add the result to equation 13 above $1 M_{\odot}$ (Bovy, pers. comm.). Because stellar number density is only important for absolute yield estimation, we skip this step.

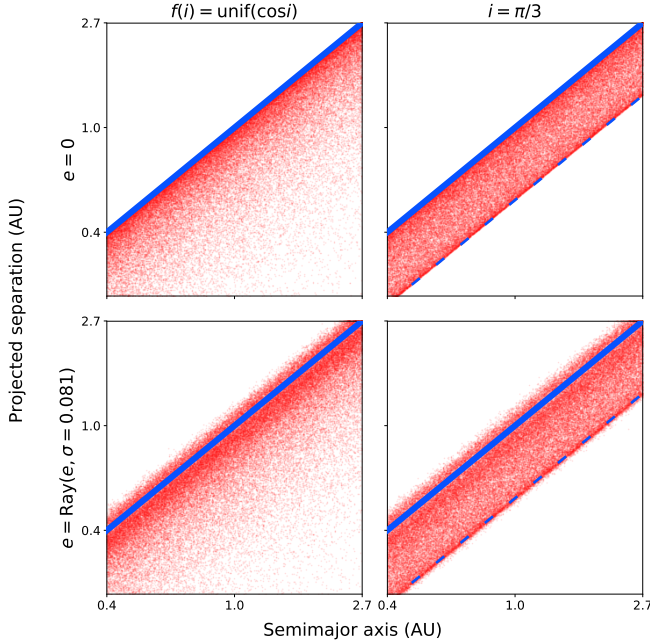


Figure 4. Density scatter plots showing the distribution of projected separation with semi-major axis for different assumptions about eccentricity and inclination distributions. The solid blue line indicates 1:1 correspondence, $a_{\text{proj}} = a$. The dashed blue line shows $a_{\text{proj}} = a \cos i$, which is the minimum a_{proj} for fixed inclination and circular orbits. The distribution of a_{proj} with a is bimodal for fixed inclination (right column) because the apparent orbital speed of the planet has minima at both $a_{\text{proj}} = a$ and $a_{\text{proj}} = a \cos i$, effectively piling-up planets at these four points on the orbit.

will also be synchronously rotating (Kasting et al. 1993). Their climates are likely quite alien (Shields et al. 2016).

We let M_* have a power law distribution, $dN/dM_* \propto M_*^{-4.7}$ (Bovy 2017). We choose a normalization such that the cumulative probability equals unity in the range $M_* = [0.67, 1.6] M_\odot$. Stellar luminosity is calculated by $L_*/L_\odot = (M_*/M_\odot)^4$. The values of $a_{\oplus, \text{min}}$ and $a_{\oplus, \text{max}}$ at star q are then scaled by the square root of $L_{*,q}$, which effectively ignores the planetary albedo dependence on wavelength (Kasting et al. 1993).

Because $a_{\oplus, \text{max}}$ sets the edge of the the search volume (equation 12), this means that the furthest K star probed for Earth twins is nearer than the furthest-probed F star. In other words, a star q is disqualified if $a_{\oplus, \text{max}, q} > r_q \times \text{IWA}$. We find that relaxing $M_* = M_\odot$ slightly increases the false positive rate, but this is probably not significant.

4.1.4. Planetary demographics

How appropriate is the assumption that radius and semi-major axis have log-uniform distributions? Estimating underlying distributions of exoplanets near $1 R_\oplus$ and 1 AU is difficult because we have observed so few

such planets. Extrapolation is required, such as in Petigura et al. (2013), whose flat distribution we implement in this study.

More recent work (Foreman-Mackey et al. 2014) extrapolates the distributions of radius and period using fewer assumptions than Petigura et al. (2013). For planets on >100 -day orbits, large radii ($10 R_\oplus$) may occur less frequently than small radii ($1 R_\oplus$), but the discrepancy is smaller than it is for shorter periods. Within the errors, however, a flat distribution does not appear to be inconsistent with Foreman-Mackey et al. (2014).

The radius distribution of short-period planets is bimodal (Fulton et al. 2017; Zeng et al. 2017), but may be shaped by atmospheric loss via evaporation (Lopez & Rice 2016). For planets in the habitable zone of G dwarfs in particular, the radius distribution is still poorly constrained. In any case, radius comes into the direct imaging signal as $A^* R^2$, where the apparent albedo A^* is unknown. Even a bimodal distribution would likely be smeared out by albedo variance.

Estimates of earth twin occurrence rate are directly tied to these period and radius distribution models. Petigura et al. (2013) present an occurrence rate $\eta_\oplus = 5.7\%$, which we divide by their Earth bin volume to get a density, $\Gamma_\oplus = 0.12$. Foreman-Mackey et al. (2014) update Petigura et al. to find $\Gamma_\oplus = 0.02$, smaller by an order of magnitude, while Hsu et al. (2018) find $\Gamma_\oplus = 1.6$, larger by an order of magnitude. We adopt the earlier Petigura et al. value because it is based on log-uniform distributions in R and a , so we can apply a constant value of Γ to all planets in our simulation, and still not conflict with previous work. The true occurrence rate may lie somewhere between these two results.

If Γ is constant—that is, if planets occur at equal rates in every bin—then the detection efficiency and its variation over R and a are divorced from the actual value of Γ_\oplus , for a volume-limited search. We are free, then, to ignore whether Γ_\oplus is closer to 0.02 or 0.12; its value is only needed to estimate yields.

However, if Γ is not constant and Γ_\oplus is lower than its neighbouring bins (Foreman-Mackey et al. 2014), then our survey would yield more false positives. Or vice versa, if Γ_\oplus is higher than its neighbours (Hsu et al. 2018; Kopparapu et al. 2018).

We tested how non-uniform demographics change our results by implementing log-normal distributions for both R and P , with μ at the respective Earth value, and σ the width of one bin. The increased abundance of Earth twins means the false positive rate is lower by a handful of percentage points, excepting the targeted scenario for a log-normal P realization (since the a - a_{proj} degeneracy is trivial).

We also prescribe an overall upper limit of $4.5 R_{\oplus}$ to the planets we generate (e.g., one e -folding above $R_{\oplus, \max}$). This may miss false positives with large radii and low albedo, or crescent phase. Hence, again, our results give a lower limit of the false positive rate.

4.1.5. Orbital eccentricity

We have assumed circular orbits, but we know precious little about the eccentricity of sub-Neptunes in long-period orbits around Sun-like stars, let alone Earth twins.

To test how non-zero eccentricity affects our results, we ran a simulation where eccentricity is drawn from a Rayleigh distribution with dispersion $\sigma = 0.081$, as given by Shabram et al. (2016) for transiting planets. Although eccentricities are especially hard to measure for small planets, reports of eccentricity-period distributions consistently show peaks around $e \approx 0$, for both transiting and radial velocity planets (Winn & Fabrycky 2015).

We find that treating e as a random parameter results in a false positive rate of 77% for a blind survey and 47% for a targeted survey, indistinguishable from our fiducial, zero-eccentricity case. We posit that this is because inclination, not eccentricity, represents the first-order control on the distribution of projected separation with semi-major axis (figure 4). We therefore conclude that our analysis is robust to the assumption of circular orbits.

4.1.6. Phase function and albedo

We have adopted the Lambertian phase curve throughout our analysis. In reality, however, a planet’s phase function will differ from the Lambertian model (Burrows & Orton 2009; Mayorga et al. 2016)—for example, Titan is strongly forward-scattering and appears brighter at larger phase angles (García Muñoz et al. 2017). Our ignorance of exoplanet phase functions is largely encapsulated in the apparent albedo, which we allow to vary by an order of magnitude.

As we have stressed throughout this work, the albedo distribution of rocky planets is wholly unconstrained. Moreover, A^* may change as we observe different regions of the planet (Cowan & Fujii 2017).

As for our assumptions about A_{\min}^* and A_{\max}^* , hot Jupiters exhibit more than an order of magnitude range in albedo (Heng & Demory 2013), despite being relatively simple planets: similar mass, size, composition, etc. There is therefore reason to believe that smaller, cooler planets, which are inherently more diverse, will exhibit a variety of different albedos.

In figure 5, we present the Earth twin false positive rate as a function of the underlying range of apparent

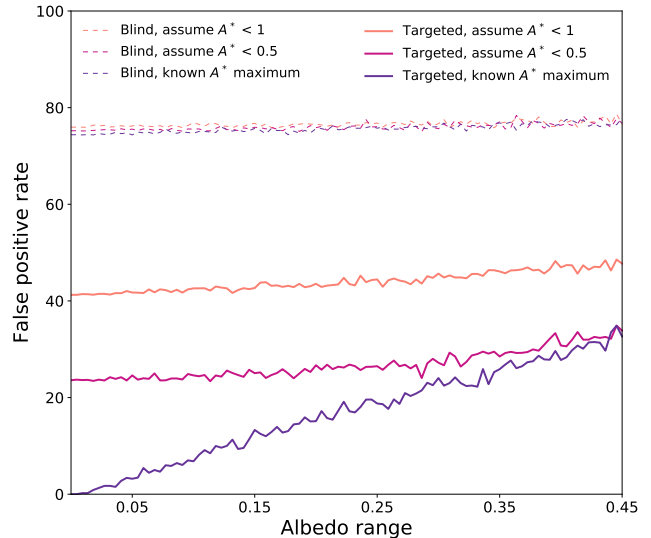


Figure 5. Effect of albedo distribution—and our knowledge thereof—on the false positive rate, or, the odds of an Earth twin candidate being an un-Earth. The x -axis is the range within which albedo is allowed to randomly vary *in the model*: the greatest range corresponds to $A^* \in [0.05, 0.5]$, and the smallest range to $A^* = 0.3$. Dashed lines represent searches for planets at random phase, while solid lines represent targeted searches. Colours show different assumed maximum albedos (e.g., the value of A^* in equation 15). Noise in this figure is due to model Poisson noise: because A^* is generated anew for each planet per albedo range increment, sometimes planets will be assigned new A^* values sufficiently low to diminish their planet/star contrasts below the instrument floor, which renders them undetectable. The false positive rate in a blind search is insensitive to the underlying albedo distribution, or our knowledge thereof (dashed lines). Targeted searches still have false positive rates of at least 1 in 2, unless all planets have the same albedo (albedo range of 0) and we know that universal albedo *a priori* (solid purple line).

albedo. The problem of unknown albedo is twofold: not only do we not know the albedos of individual planets, but we do not even know the albedo *distribution* of planets at 1 AU. Therefore, we are left with (i) our best guess for A_{\max}^* (which affects the extent of the Earth twin candidate zone), as well as (ii) our luck in nature’s range of A^* being on the small side.

The Earth twin false positive rate varies with both of these estimates. If every candidate planet had the same albedo and phase function *and* we knew the universal albedo and phase function *a priori*, then—and only then—would a targeted search return a 0% false positive rate, since the radius-albedo degeneracy would be broken. As the universe’s underlying distribution widens, however, our knowledge of the albedo maximum gives us less and less of an advantage.

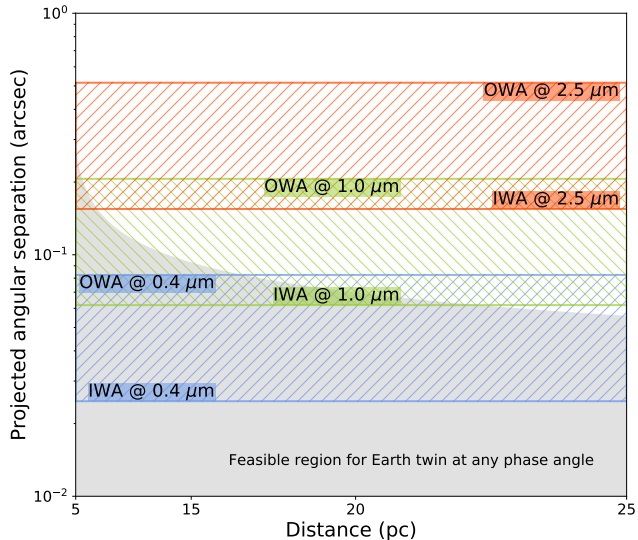


Figure 6. Inner and outer working angles at various wavelengths (horizontal lines), for a 10-m telescope with an IWA of $3\lambda/D$ and an OWA of $10\lambda/D$. Hatched regions represent where an exoplanet would be unobscured. The angular projected separation for an Earth twin, as a function of distance, is shown by the grey region. Targets are only visible at some wavelength if the grey swath intersects a wavelength’s working angle box. The hatched regions have little-to-no overlap, meaning that no planets can be simultaneously imaged from 0.4 to 2.5 μm , and a full spectrum can only be stitched together for the very nearest and most inclined planets. Because the x -axis is scaled to constant volume per centimetre, this demonstrates that the vast majority of Earth twins have too tight a projected angular separation for longwave characterization.

Table 2 shows that adopting an underlying normal distribution for A^* ($\mu = 0.3$, $\sigma = 0.1$) also reduces the false positive rate of a targeted search, in a similar way to shortening the range of A^* .

4.1.7. Wavelength and working angles

Inner and outer working angles depend directly on imaging wavelength. Shorter wavelengths will tighten the working angles, while longer wavelengths will push them to wider separations. The wavelength we choose to work with thus affects which planets are obscured and which are not. Our adoption of 1.0 μm dictates that planets are obscured more often than the 0.55- μm assumption of Stark et al. (2014). Indeed, Stark et al. (2015, 2016) require that planets are simultaneously detectable at 0.55 and 1.0 μm . Regardless, the false positive rate is roughly insensitive to both the wavelength and the working angles themselves (table 2).

If we want to spectroscopically characterize the atmospheres of planets we detect, then we require observations at multiple bands. For full characterization, we

would hope for a spectrum ranging from 400 nm in the shortwave (Rayleigh scattering), to 2.5 μm in the longwave (greenhouse gas absorption, e.g. methane).

Directly imaging a planet at multiple wavelengths is not trivial, however, due to chromatic working angles. We illustrate this in figure 6 by showing the projected angular separations at which an Earth twin might appear, overlain by the working angles at some different wavelengths.

If we want to *simultaneously* detect a planet at multiple wavelengths, then the regions bounded by the relevant IWAs and OWAs *and* the planet’s angular separation must all overlap somewhere. As figure 6 shows, this is unfortunately not achievable for 400 nm and 2.5 μm , if $\text{OWA} = 10\lambda/D$ and $\text{IWA} = 3\lambda/D$. Parallel coronagraphs, with different IWAs and OWAs, are a possibility for imaging more planets at such a range of wavelength bands.

Thus we may be forced to attempt stitching together observations taken at different phases, at least for planets on inclined orbits. This raises practical challenges, since $\phi(\alpha)$ varies with wavelength; phase variations are likely chromatic (Cahoy et al. 2010; Mayorga et al. 2016). Further—and this extends to all of Earth twin spectroscopy—we are chasing moving targets. The integration time required to characterize an Earth twin could be on the scale of months (Robinson et al. 2016), and a planet on a 1-AU orbit will surely move during this time.⁸ It may therefore be necessary to acquire orbital constraints before obtaining spectra.

Regardless, even with snapshots at several orbital phases, figure 6 illustrates that only the nearest ($r \lesssim 9$ pc) Earth twins are possibly observable both at 400 nm and 2.5 μm . Of the simulated Earth twins detectable at 400 nm, 23.9% are detectable at 1.0 μm at any phase, and only 0.6% at 2.5 μm .

One debatable solution is to use a starshade, rather than a coronagraph, to obtain spectra of Earth twin atmospheres. The IWA of a starshade depends on the starshade radius divided by the starshade-telescope distance, and its OWA is simply the field of view. This results in a greater unobscured range of separations. Starshades also have greater bandwidth, so obtaining a full spectrum requires fewer passes. However, because starshade slew time is long, fewer stars can be targeted, and starshades themselves pose different technical challenges.

⁸ A planet with $a = 1$ AU at $r = 10$ pc would move 5 pixels over a 30-day integration, assuming a Nyquist-sampled pixel scale and a 10-m telescope. The same planet at $r = 20$ pc would move 2.5 pixels.

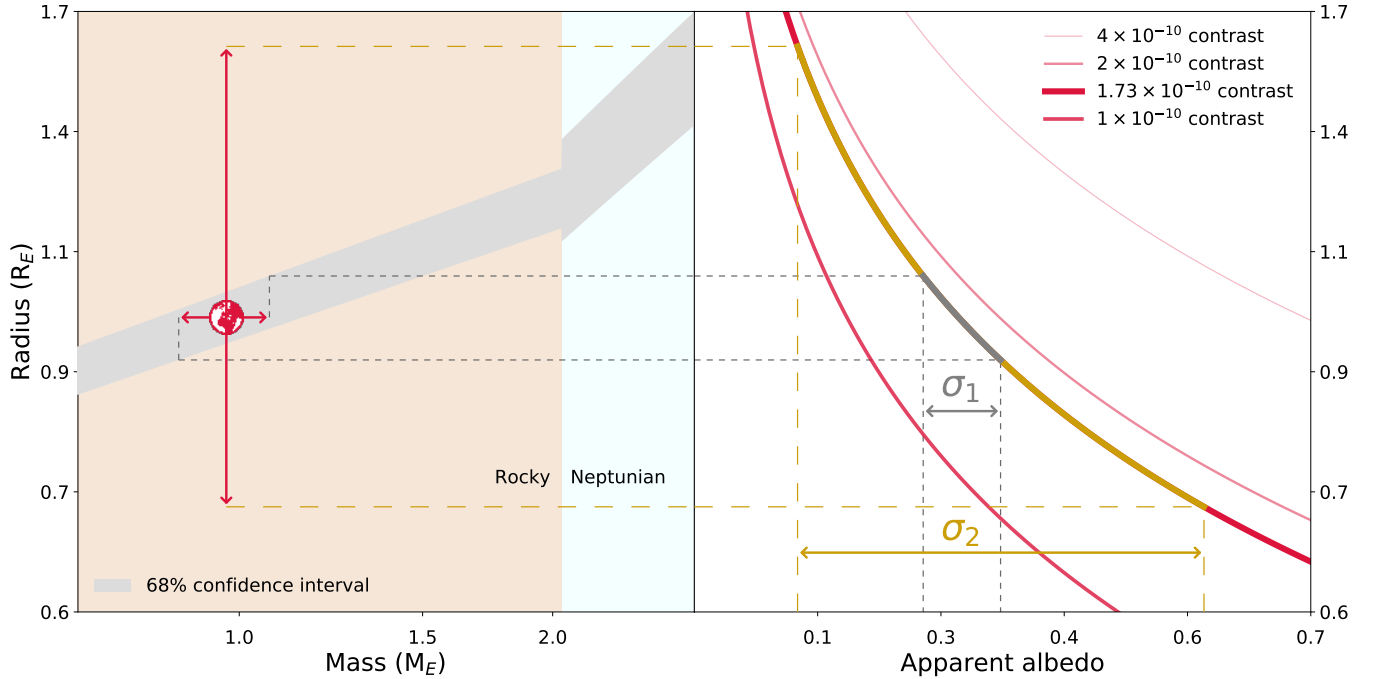


Figure 7. *Left:* Planetary mass-radius relation from [Chen & Kipping \(2017\)](#). Grey swath shows 68% confidence interval. Horizontal error bars are the hypothetical mass measurement error, here set at a very optimistic value of 10% (e.g., using 1 cm/s precision radial velocity; [Plavchan et al. 2018](#)). Vertical error bars show a hypothetical radius constraint retrieved from a Rayleigh scattering spectrum ([Feng et al. 2018](#)). The dashed lines show 1σ radius constraints, where grey lines correspond to the mass constraint and ochre lines correspond to the spectral retrieval constraint. *Right:* radius-albedo degeneracy at a constant planet/star contrast of 1.73×10^{-10} (bold line), which corresponds to an Earth twin at quadrature and 1 AU separation. Other lines show different planet/star contrasts for the same phase and separation. The error on radius, as estimated from mass/or from spectral retrieval, directly propagates to an error on albedo. We might then estimate albedo to within roughly $\pm 0.05(\sigma_1)$ or $\pm 0.25(\sigma_2)$, respectively, for planets with Earthlike albedo and radius.

4.1.8. Multiple observations

Our blind search model assumes one observation per star, while our targeted search assumes either precursor orbit constraints, or enough direct imaging visits per star to fully constrain planetary orbits. A realistic mission will fall between these endmembers—at a given point, we may have visited a star more than once, yet possibly not enough times to precisely know the semi-major axis of the hosted planet(s). This raises an interesting question: how does the false positive rate change with each additional visit to the same star? The answer requires knowing the most efficient timing of visits, an important area of future research. For now, we posit that our false positive rates reported for the blind and targeted scenarios represent upper and lower bounds, respectively.

4.2. Breaking the radius-albedo degeneracy

We consider two possible routes to constraining planetary albedo (figure 7). One route is to choose targets whose masses are known from radial velocity or astrometry surveys ([Plavchan et al. 2018](#); [Shao et al. 2018](#);

[Bendek et al. 2015](#); [Fischer et al. 2016](#); [Weiss et al. 2016](#)). We can use a mass-radius relation (e.g., [Chen & Kipping 2017](#)) to estimate the planet’s radius from its mass. This is a risky endeavour, as current mass-radius relations are necessarily for short-period planets and therefore may not be representative of Earth twins. A corollary benefit of targeting known-mass planets is that their orbits would have been constrained along with mass. This would inform us of which stars to target and when to look.

The second route takes advantage of Rayleigh scattering. [Feng et al. \(2018\)](#) showed that modeled Rayleigh scattering spectra are independent of surface albedo, and could therefore constrain radius. In theory, if we measure the Rayleigh scattering spectrum of a planet at known phase, then we can estimate its radius.

This retrieval is more complicated for an atmosphere with clouds. However, the longer atmospheric path-lengths at crescent phase mean that surface and cloud scattering are less important at these phase angles. Thus, reflected light at crescent phase is—in principle—

closer to pure Rayleigh scattering, and hence might constrain radius, even for cloudy atmospheres.

Figure 7 shows that a 10% constraint on mass would propagate to approximately a $\pm 0.1 R_{\oplus}$ constraint on radius and a ± 0.05 constraint on albedo, for Earthlike planets at 1 AU, and that a 50% radius constraint from a Rayleigh scattering spectrum would propagate to an ± 0.25 constraint on albedo. A precise value of σ_{A^*} is not reported because this error would be dominated by systematic errors; e.g., using a mass-radius relationship for short period planets.

5. CONCLUSIONS

We have performed Monte Carlo simulations of reflected light direct imaging surveys adopting a simple telescope model. Our main finding is: if we image stars at random, $\sim 77\%$ of the detected planets that appear Earthlike in separation and planet/star contrast will in fact not be Earth twins. Meanwhile, $\sim 88\%$ of Earth twins go undetected within our search volume of 22.6 pc, although this depends on model assumptions; namely, the maximum survey distance in our volume-limited survey.

We can double the chances that detected Earth candidates are true Earth twins—and triple the chances of seeing Earth twin planets, on average—by only targeting known planets. Yet even then we cannot do better than a $\gtrsim 50\%$ false positive rate, as our capacity to know whether a planet is an Earth twin is set by our knowledge of the albedo distribution of rocky planets at

large semi-major axes. These two estimates of the false positive rate represent endmember search scenarios, in which we either know nothing or everything about the orbits of the imaged planets. The false positive rate of a realistic direct imaging mission would fall in between these values.

Our results are robust to working angle geometry (including imaging wavelength), to the assumption of non-circular orbits, to the inclusion of F and K stars, and to the underlying radius, period, and albedo distributions of planets.

Breaking the radius-albedo degeneracy should be a focus of research before choosing Earth twin candidates for costly spectroscopic characterization. We may be able to constrain a planet’s radius from its mass, motivating cooperation between direct imaging and radial velocity and astrometry.

This work is supported by the McGill Space Institute and the Technologies for Exo-Planetary Science training program. We show our gratitude to the LUVUOIR STDT for their useful conversation, to the Exoclipse meeting attendees and organizers for the feedback received on a preliminary presentation of this work, to M. Marley and T. Robinson for enlightening discussion on the radius-albedo degeneracy, and to an anonymous referee, whose comments greatly improved the scientific quality of this manuscript. CMG thanks T. Bell, L. Dang, and D. Keating for additional discussion. Lastly, NBC acknowledges the support of the Canadian Space Agency towards attending LUVUOIR meetings.

REFERENCES

- Agol, E. 2007, MNRAS, 374, 1271
- Bate, M. R. 2009, MNRAS, 392, 590
- Bendek, E., Ammons, M., Bennett, D., et al. 2015, UV-VIS-APRA Workshop presentation
- Bovy, J. 2017, MNRAS, 470, 1360
- Brown, R. A. 2005, ApJ, 624, 1010
- Burrows, A., & Orton, G. 2009, Giant Planet Atmospheres and Spectra, ed. S. Seager
- Butler, R. P., Vogt, S. S., Laughlin, G., et al. 2017, AJ, 153, 208
- Cahoy, K. L., Marley, M. S., & Fortney, J. J. 2010, ApJ, 724, 189
- Chen, J., & Kipping, D. 2017, ApJ, 834, 17
- Cowan, N. B., & Fujii, Y. 2017, ArXiv e-prints, arXiv:1704.07832
- Dalcanton, J., Seager, S., Aigrain, S., et al. 2015, ArXiv e-prints, arXiv:1507.04779
- Dooley, J., & Lawson, P. 2005, Technology Plan for the Terrestrial Planet Finder Coronagraph, Tech. Rep. 05-8, Jet Propulsion Laboratory, California Institute of Technology
- Feng, Y. K., Robinson, T. D., Fortney, J. J., et al. 2018, ArXiv e-prints, arXiv:1803.06403
- Fischer, D. A., Anglada-Escude, G., Arriagada, P., et al. 2016, PASP, 128, 066001
- Ford, E. B., Seager, S., & Turner, E. L. 2001, Nature, 412, 885 EP
- Foreman-Mackey, D., Hogg, D. W., & Morton, T. D. 2014, ApJ, 795, 64
- Fulton, B. J., Petigura, E. A., Howard, A. W., et al. 2017, AJ, 154, 109
- García Muñoz, A., Lavvas, P., & West, R. A. 2017, Nature Astronomy, 1, 0114

Table 3. Definitions of symbols used in this text. Listed values correspond to the fiducial case; many of these parameters are varied in our sensitivity analysis.

Randomly-generated planetary parameters							
Symbol	Min	Max	Units	Description	Probability distribution	Eqn.	
R	0.6	4.5	R_{\oplus}	Planetary radius	Uniform in $\ln(R)$	5	
a	0.37	2.72	AU	semi-major axis	Uniform in $\ln(a)$	6	
ξ	0	2π	rad	Orbital phase	Uniform	7	
i	0	$\pi/2$	rad	Orbital inclination	Uniform in $\cos(i)$	8	
A^*	0.05	0.5	-	Planetary apparent albedo	Uniform	10	
r	0	22.6	pc	Distance between star system and observer	Uniform in r^2	11	
Derived planetary parameters							
Symbol			Units	Description		Eqn.	
ε			-	Planet/star contrast ratio		1	
$\phi_L(\alpha)$			-	Lambertian phase function		2	
α			rad	Phase angle between planet and observer		3	
a_{proj}			AU	Projected separation		4	
ε'			-	Phase-normalized planet/star contrast ratio		15	
Free model parameters							
Symbol	Value		Units	Description			
ε_{min}	1.0×10^{-10}		-	Coronagraph raw planet/star contrast ratio			
$R_{\oplus, \text{min}}$	0.6		R_{\oplus}	Minimum radius for Earth twin classification			
$R_{\oplus, \text{max}}$	1.6		R_{\oplus}	Maximum radius for Earth twin classification			
$a_{\oplus, \text{min}}$	0.72		AU	Minimum semi-major axis for Earth twin classification			
$a_{\oplus, \text{max}}$	1.40		AU	Maximum semi-major axis for Earth twin classification			
Γ_{\oplus}	0.119		nat^{-2}	Earth twin occurrence rate density			
M_*	1		M_{\odot}	Mass of host star			
D	10		m	Telescope primary aperture diameter			
λ	1.0		μm	Imaging wavelength			
N_{in}	3		-	Number of λ/D at coronagraph inner working angle			
N_{out}	10		-	Number of λ/D at coronagraph outer working angle			

Guyon, O. 2011, in European Physical Journal Web of Conferences, Vol. 16, European Physical Journal Web of Conferences, 03001

Heller, R., Leconte, J., & Barnes, R. 2011, A&A, 528, A27

Heng, K., & Demory, B.-O. 2013, ApJ, 777, 100

Hsu, D. C., Ford, E. B., Ragozzine, D., & Morehead, R. C. 2018, ArXiv e-prints, arXiv:1803.10787

Kasting, J. F., Whitmire, D. P., & Reynolds, R. T. 1993, Icarus, 101, 108

Kopparapu, R. k., Hebrard, E., Belikov, R., et al. 2018, ArXiv e-prints, arXiv:1802.09602

Krissansen-Totton, J., Schwieterman, E. W., Charnay, B., et al. 2016, ApJ, 817, 31

Kroupa, P., & Burkert, A. 2001, ApJ, 555, 945

Lopez, E. D., & Rice, K. 2016, ArXiv e-prints, arXiv:1610.09390

Marais, D. J. D., Harwit, M. O., Jucks, K. W., et al. 2002, Astrobiology, 2 2, 153

Mayorga, L. C., Jackiewicz, J., Rages, K., et al. 2016, AJ, 152, 209

Petigura, E. A., Howard, A. W., & Marcy, G. W. 2013, Proceedings of the National Academy of Science, 110, 19273

Plavchan, P., Cale, B., Newman, P., et al. 2018, ArXiv e-prints, arXiv:1803.03960

Ranalli, P., Hobbs, D., & Lindegren, L. 2017, ArXiv e-prints, arXiv:1704.02493

- Rauscher, B., Bolcar, M., Clampin, M., et al. 2015, in Proc. SPIE Optics + Photonics 2015, International Society for Optical Engineering
- Roberge, A., Chen, C. H., Millan-Gabet, R., et al. 2012, *PASP*, 124, 799
- Robinson, T. D., Stapelfeldt, K. R., & Marley, M. S. 2016, *PASP*, 128, 025003
- Rogers, L. A. 2015, *ApJ*, 801, 41
- Shabram, M., Demory, B.-O., Cisewski, J., Ford, E. B., & Rogers, L. 2016, *ApJ*, 820, 93
- Shao, M., Turyshev, S. G., Bendek, E., et al. 2018, ArXiv e-prints, arXiv:1803.03732
- Shields, A. L., Ballard, S., & Johnson, J. A. 2016, *PhR*, 663, 1
- Stark, C. C., Roberge, A., Mandell, A., et al. 2015, *ApJ*, 808, 149
- Stark, C. C., Roberge, A., Mandell, A., & Robinson, T. D. 2014, *ApJ*, 795, 122
- Stark, C. C., Shaklan, S. B., Lisman, P. D., et al. 2016, *Journal of Astronomical Telescopes, Instruments, and Systems*, 2, 2
- Traub, W. A., & Oppenheimer, B. R. 2010, in *Exoplanets*, ed. S. Seager, 111–156
- Weiss, L. M., Rogers, L. A., Isaacson, H. T., et al. 2016, *ApJ*, 819, 83
- Winn, J. N., & Fabrycky, D. C. 2015, *ARA&A*, 53, 409
- Zeng, L., Jacobsen, S. B., & Sasselov, D. D. 2017, ArXiv e-prints, arXiv:1712.05458